

Acoustic Localisation of Chafer Beetle Larvae

Candidate Number: 8211Q
NST: Part III Physics
University of Cambridge
Supervisor: Dr Christopher Lester

Abstract

The detection of insects via acoustic means has long been a field of interest since the early 1990's. The presence of insects in soil, grains and plant bodies have been successfully been detected using various techniques including the use of sensitive accelerometers, electret microphones and laser doppler vibrometers. However, little attempt has been made to precisely locate the insects owing to limited understanding of how wave propagates through soil and due to the nature of soil as a highly dispersive medium. In this work, we highlight the major difficulties in detecting insects in soil by conducting an experiment on a model system consisting of a piezoelectric speaker as the sound source and an electret microphone as the detector. It was found that while the speed of sound measured in air using the model system was determined to be $(344 \pm 1) \text{ m s}^{-1}$, in agreement with known values, the attenuation of sound displays a more complicated behaviour, preventing the attenuation coefficient from being determined. In the latter half of the work, the range of detection was quantified and mapped out for different values of soil saturation and wave frequencies. For frequencies corresponding to the range present in the spectral analysis of chafer beetle recordings, the range of detection was of order 50 cm for all values of soil saturation. This limited range confirms the difficulty in detecting the weak signals produced by soil dwelling insects.

Impact of Covid-19

The shutdown of the laboratory due to Covid-19 meant that I had to shift the focus of my project which I originally intended to be an experimental one. The main focus of my project pre-lockdown was on determining the wave properties of sound waves propagating in soil. I had reached a stage where the device which I had to build from scratch was ready for measurement as I highlighted in my report. The calibration of the instruments and measurement of speed and attenuation of the wave in air shows that the same techniques are transferable to measurements in soil.

The result of the lockdown is that I had to incorporate a larger portion of the theoretical modelling of soil, shifting the project to a more computational one. This meant having to study an extra theoretical model and included the need to code an implementation of the model. I had hesitated to do this at first during the uncertain period when the university was in the amber phase and instead focused my efforts on preparing to move my experimental set-up home, with incredibly helpful guidance from Richard King, the Undergraduate Laboratory Manager. Roughly one week was spent planning and moving at this stage.

Once it was clear that shutdown of the laboratory was unavoidable, as an international student, I faced the dilemma of whether to stay in the UK or relocate to Thailand. I preferred to stay as I knew that relocating to Thailand would mean more time wasted having to pack up and leave the UK for good which is no small task. As I had moved away from home in Thailand for 6 years now, the space is no longer suitable for work due to the lack of quiet space and the lack of a desk. Despite all these factors, there was immense pressure to return home from concerned family members so everyday was a constant debate.

To summarise, Covid-19 meant that my original plans to complete my experiment were derailed and I had to switch tracks to a more computational project. The uncertainty in whether to return to Thailand meant that extra time and energy was spent on that difficult decision.

Contents

1 Introduction	3
2 Characteristic Signal of Chafer Grubs	3
2.1 Insect and Background Noise	4
2.2 Comparing Different Insect Species	4
3 Microstructural Parameters of Soil	4
3.1 Porosity	5
3.2 Saturation	5
4 Material and Methods	5
4.1 Signal Output	5
4.2 Function Generator Frequency Sweep	5
4.3 Sound and Vibration Sensor	6
4.4 Filtering and Minimising Noise	6
4.5 Differential Amplifier	7
4.6 Taking Measurements	7
5 Results and Discussion	7
5.1 Calibration	7
5.2 Signal-to-noise Ratio	7
5.3 Speed Measurement	8
5.4 Attenuation Measurement	8
6 Soil as an Unsaturated Porous Medium	9
6.1 Capillary Pressure	9
6.1.1 Permeability	10
6.2 Material Parameters	10
6.3 Three-Component Model	11
7 Wave Propagation	12
7.1 Dispersion Relations	12
8 Simulation of Detection Range	13
8.1 Frequency Dependence	13
8.2 Saturation Dependence	13
9 Detection Range Map	13
10 Conclusion	13

1 Introduction

Lawns require regular attention and are often susceptible to damage caused by pests residing beneath the turf. Among the most common lawn pests in the UK are the chafer beetle grubs [2]. The adult stage of the beetle is not a threat to the lawn but their root-feeding larvae eat away at the roots of the grass, resulting in dead patches which can be peeled away from the soil surface [24]. These grubs often escape detection until significant visible damage had occurred.

Since the early 1990's, it has been shown that insects produce vibrations in the infested medium through feeding and burrowing processes which can be picked up using acoustic detection methods. Previous work included the use of sensitive accelerometers, electret microphones

or laser doppler vibrometers to detect insects in various media such as grains, wood and plant bodies [18, 20, 13]. In soil, notable work involved using a steel stake inserted into the sampling site with an accelerometer magnetically attached to the free end [11]. Though these previous efforts have established techniques of mapping out infestation sites and even estimating the population density [3, 15] precisely locating the grubs has proved to be a challenge.

One major obstacle is the detection of weak insect signals in noisy environments [26, 18, 17]. To better understand the factors limiting the localisation of chafer beetle larvae in lawns, I built and studied a model system consisting of a piezoelectric speaker and a series of electret microphone buried in soil. The speaker acts as the noisy sound source while the microphones record the signal. The aim of the experiment was to determine the characteristics of the insect signal that allow it to be distinguished from noise and to investigate whether the location of the source could be triangulated using multiple detectors.

Owing to the Covid-19 situation, exceptional circumstances prompted a decision to be made to halt the experimental aspect of the work before the system could be tested in the soil sample. Though diverting from the original aim, an important aspect of the detection device is the range of detection. Postulating that the range of detection depends on the frequency of the sound wave being transmitted as well as the microstructural properties of soil such as saturation and porosity, I conducted a numerical investigation of sound propagation through porous media. Using supporting data obtained from the model system built, I mapped out the conditions under which a practical range of detection can be achieved.

In this paper, I outline the experimental methods for measuring acoustic signals in soil and discuss results from the numerical simulation of wave propagation in porous media, as applied to a frequency range matching that of insect-produced vibrations. The paper is organised into eight sections. The first two sections define the signal of interest and the soil properties affecting wave propagation. The next two sections are dedicated to the construction and calibration of an acoustic measurement device. Three sections detail a theoretical model for soil and the numerical results for the wave speed, attenuation and detection range for different signal frequencies and soil saturation values. In the final section, I consider the implications of the findings on acoustic methods as a means for pest detection.

2 Characteristic Signal of Chafer Grubs

Work by Mankin et al. lays the foundation for the acoustic detection of soil-dwelling insects such as the chafer grubs by providing spectral comparisons between the sounds produced by different species of insects. These

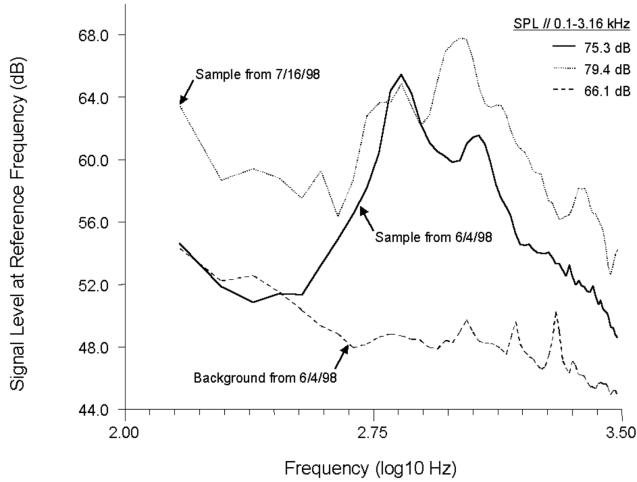


Figure 1: Comparison of chafer beetle acoustic spectrum and quiet background. Adapted from Mankin et al. [17]

acoustic profiles were also shown to be distinguishable from that of other sources of background noise in the field such as wind and traffic noise, both in the time and frequency domain [17].

2.1 Insect and Background Noise

Subterranean insects produce brief broadband vibrational impulses as a result of their movement and feeding. It was shown that these bursts of impulses have a distinct spectral profile from wind and traffic noise [22]. Figure 1 shows the power of the field recording of quiet seismic background noise decreasing with frequency. The quiet background noise is contrasted with two spectral profiles of insect (*D. abbreviatus*) recordings sampled at two different dates. The background noise has a much lower amplitude than the signal of interest at high frequencies.

A comparison of louder background noises due to wind and vehicles with that of the white grubs is shown in Figure 2. Here, the spectral profile of the background noise is broadband and therefore has significant contributions even in the higher frequency region. It can be noted, however, that while the signal level remains roughly the same across the entire frequency range for the beetles, there is a significant drop in power going from the low frequency to high frequency region in the wind and truck spectra. By comparing the ratio of the power below 400 Hz and that above for each spectrum, the background noise can be distinguished from the insect noise.

2.2 Comparing Different Insect Species

In Figure 3, the Fourier spectra of different species of insects were compared. Each of these spectra are broadband between 0.1 kHz to 3.16 kHz and therefore the sound of chafer grubs cannot be reliably distinguished

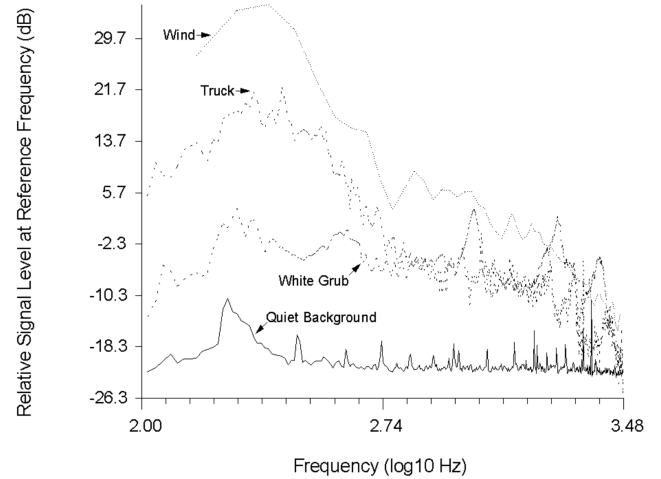


Figure 2: Comparison of chafer beetle acoustic spectrum, vehicle noise and wind noise. Adapted from Mankin et al. [17]

from other species. The broadband feature suggests that the detected sounds are not species-specific communication signals, known as stridulation [8], but rather are produced through burrowing and feeding activities [17].

These findings show that while the quiet background noise does not present a problem for detection, louder noises due to passing vehicles and wind are more challenging to exclude. Detection can however be conducted during quieter hours with less vehicles. Though it is not possible to distinguish between different insect species using their frequency spectra, once located, more accurate recordings can be made at the site of infestation to listen for the quieter stridulations.

3 Microstructural Parameters of Soil

The signal produced by the chafer grub travels through soil to reach the detector. In the model system used in the experiment, the property of the soil can be varied in two different ways, by varying how wet and compact the soil sample is. Here, we discuss how these microstructural properties are quantified.

Soil is a porous medium through which water, gas and solutes can move. The solid skeleton of soil is typically composed of sedimentary materials such as sandstone, peat soil, granular soil, clay or limestone depending on the soil type. In Cambridge, the soil composition is a mixture of freely draining lime-rich loamy soil and lime-rich clayey soil with impeded draining [1, 25]. The soil selected for this study is loamy clay soil representative of that found in the area.

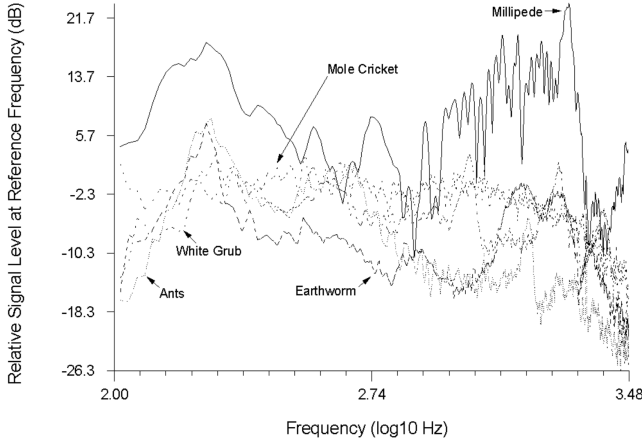


Figure 3: Comparison of insect spectra. While the quiet background noise does not present a problem for detection, louder noises due to passing vehicles and wind are more challenging to exclude. Adapted from Mankin et al. [17]

3.1 Porosity

Porosity is a measure of how much space there is between the soil grains. It is defined as the ratio of volume of void, either filled by a single pore fluid or a mixture of immiscible fluids, to the entire representative volume element (RVE). The RVE is a concept in continuum mechanics that allows heterogeneous materials to be modelled as a continuous body [10]. The RVE is defined as the volume that effectively includes a sampling of all microscopic heterogeneity and yet remains small enough to be considered a volume element.

$$n = \frac{V_{\varnothing}}{V_{RVE}}$$

where n is the porosity, V_{\varnothing} is the volume of void within the RVE and V_{RVE} is the volume of the RVE.

3.2 Saturation

In naturally occurring soil samples, the pore space between the solid grains is in general filled with at least two immiscible fluids, namely air and water, unless the soil is saturated in which case the entire pore space is occupied by water. Saturation is defined as the ratio of the volume of a single phase of pore fluid over the entire volume of void within an RVE. The sum of the degree of saturations over all fluid types is by definition equal to one.

$$S^{\theta} = \frac{V^{\theta}}{V_{RVE}} \quad \text{where } \theta \in \{F, G\}$$

where S is the saturation, V is the volume and the subscript indices F and G denote variables relating to water and air respectively. From this point onwards, as we are dealing only with water and air as our two pore fluids, we shall drop the θ suffix and define the degree

Table 1: caption

n	R_n (k Ω)	C_n (F)
L	2.2	1×10^{-7}
1	0.64	47×10^{-6}
2	1.5	3.30×10^{-7}
3	1.5	5×10^{-9}
4	2.2	
5	680	

of saturation for water as S and therefore it follows that the degree of saturation for air is $1 - S$.

4 Material and Methods

In this section, I outline the method used to build a device that would detect signal from a source buried in a medium. Though the experiment had not reached the stage of triangulating a buried sound source, useful techniques to measure wave properties in the medium were developed. Firstly, the technical specifications for each major component of the device are discussed followed by details of the signal processing circuit. I then propose a method to measure the speed and attenuation of waves in soil.

The speed and attenuation of sound were measured using a piezoelectric speaker (*Sonitron Blue Line SPS-29-T00*) and an electret condenser microphone (*Kingstate KECG2738PBJ-A*) connected to a signal processing circuit. Circuit components were selected to bandpass filter and amplify the signal received by the microphone. The full circuit diagram is shown in Figure 4. The values of the components used are summarised in Table 1. For investigating the method for measuring attenuation and speed of sound, a pure sinusoidal wave with variable frequency is used.

4.1 Signal Output

The signal is output through the *SPS-20-T00* speaker. Figure 5 shows the sound pressure level against frequency. The speaker is designed to operate in the constant output region between 1 kHz to 20 kHz. The input to the speaker is connected directly to a function generator.

4.2 Function Generator Frequency Sweep

Black Star Jupiter 2000 was used as function generator powering the speaker. The peak-to-peak voltage output was held constant for maximum sound pressure output. The function generator permits a constant D.C. control voltage input that varies the output frequency. This provides a means for a data acquisition technique using *LabVIEW* software together with an *Arduino UNO*

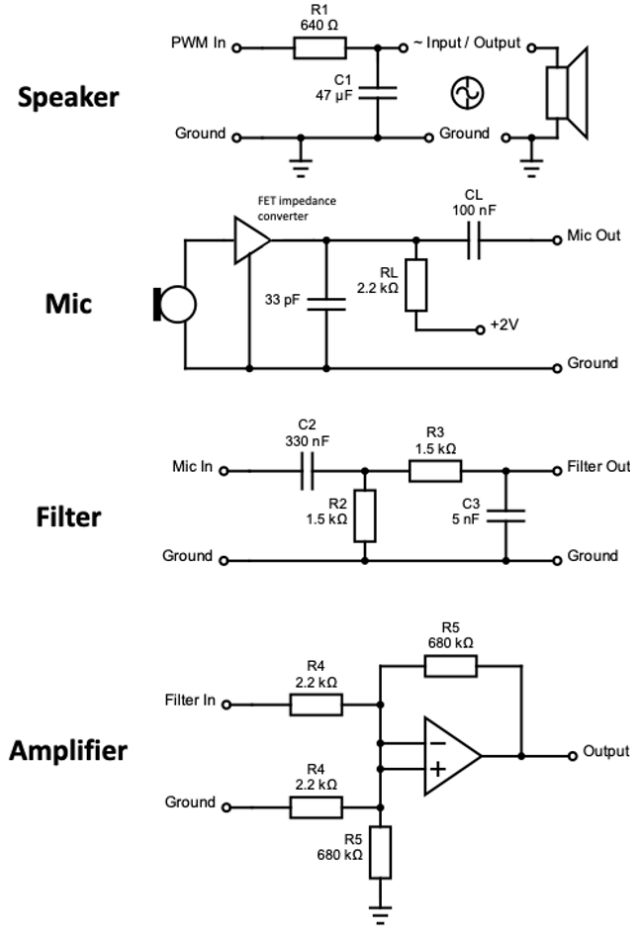


Figure 4: Circuit diagram showing the circuits used for signal processing.

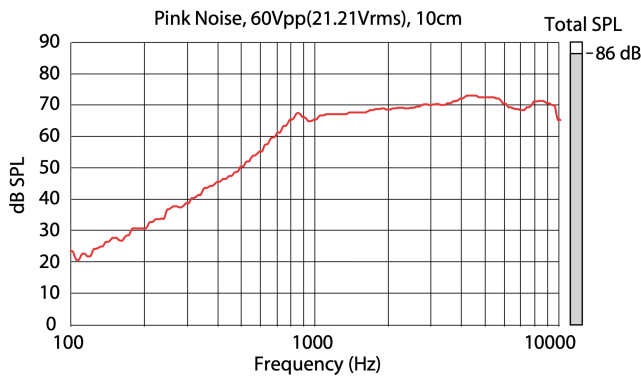


Figure 5: Response behaviour of the speaker component against frequency. Adapted from SPS-20-T00 Datasheet

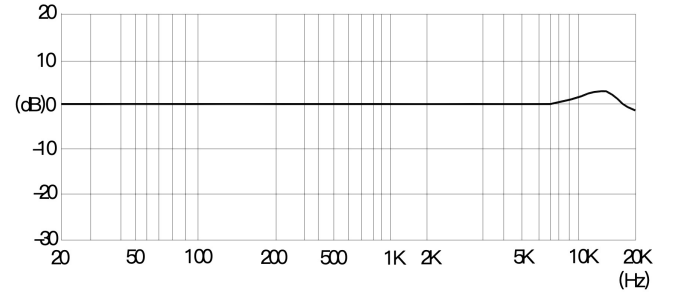


Figure 6: Sensitivity of the electret microphone against frequency. Adapted from Kingstate KECG2738PBJ-A Data Sheet.

to electronically control the frequency setting and automatically record data (see Section 4.6).

The control voltage was set using an *Arduino UNO* to vary between 0 V to 5 V. As illustrated by the speaker circuit in Figure 4, the *Arduino UNO* output is a pulse-width modulated (PWM) D.C. signal. This was converted to a constant D.C. voltage by passing through a low-pass RC filter. The filter was chosen to have a cut-off frequency of 5 Hz. We note that the function generator has a finite input impedance $Z_{in} = 9 \text{ k}\Omega$ and therefore the combined behaviour of the filter-generator circuit is not that of an ideal low-pass filter. The voltage measured across the capacitor $C1$ will be proportional to the combined impedance of the capacitor and the function generator in parallel. The resulting control voltage is given by the potential divider equation $V_C = V_{mean} Z_{C,in} / (Z_{C,in} + R1)$ where $Z_{C,in} \leq 9 \text{ k}\Omega$ is the combined impedance, V_{mean} is the mean voltage of the PWM signal passed to the filter and $R1$ is the resistance of the fixed resistor. To utilise the full range of the signal, we see that it must be the case that $R1$ is chosen to be much less than $9 \text{ k}\Omega$.

Settings on the function generator were selected to allow the frequency to vary between the range 1 kHz to 10 kHz corresponding to the linear response region of the speaker and microphone system.

4.3 Sound and Vibration Sensor

An electret condenser microphone (*Kingstate KECG2738PBJ-A*) was used as a transducer to convert the sound pressure to measurable signal. Sensors of this type have been shown by Mankin et al. (2000) [16] to be a suitable low-cost alternative to highly sensitive accelerometers, for the application of insect detection. The voltage output of the microphone is proportional to the sound pressure. Figure 6 shows the sensitivity against frequency.

4.4 Filtering and Minimising Noise

The detected signal is band-limited and therefore a bandpass filter was designed by passing the microphone output through a high-pass and low-pass RC fil-

ter (Fig. 4) with cut-off frequencies equal to 0.3 kHz and 21.2 kHz. The filter heavily suppresses components that do not lie in between these cut-off frequencies.

It is possible that the sound emitted by the speaker would bounce off walls and nearby objects so care was taken to conduct the experiment away from obstacles. The effects of noise due to magnetic fields in the environment were minimised by twisting long wires connecting the speaker and microphone to the signal processing circuit. Any noise introduced in one wire equally affects the other wire tracing approximately the same path in space and therefore measurement of potential difference across the terminals of the microphone is unaffected by such noise.

4.5 Differential Amplifier

It is necessary to amplify the weak output from the microphone before digitising and recording the signal. A differential operational amplifier circuit (Fig. 4) was chosen for this task. The amplifier compares the signal at its two inputs and amplifies the difference between them. The differential measurement has an advantage over a simple inverting amplifying circuit where the positive input is connected to ground and the negative input is amplified. Any noise common to the both inputs are ideally cancelled out in the process.

The differential amplifier has an output given by:

$$V_{out} = \frac{R5}{R4}(V_+ - V_-)$$

where V_{out} is the output from the amplifier, V_+ and V_- are the voltage inputs at the non-inverting (+) and inverting (-) input terminals respectively and the ratio $R5/R4$ is defined as the differential gain.

The output from the microphone was amplified with a differential gain of 310 to produce an appreciable signal while avoiding clipping when measured using an oscilloscope. It is worth noting that an ideal differential amplifier features two sets of two identical resistors which necessarily have exactly the same value. In practice, this is not the case and the amplifier will have a finite, non-zero gain for the quantity $(1/2)V_+ + V_-$ defined as the common mode in addition to the desired differential gain. Ideally, this gain is much less than the differential gain.

4.6 Taking Measurements

Due to time constraints, the measurement techniques that will be discussed below were developed and conducted in air, omitting the need for soil preparation. The aim of conducting these measurements was to determine the attenuation coefficient and the speed of the wave in the medium. For waves travelling through a dispersive medium such as soil, these quantities are frequency dependent.

The signal generating system was set up such that the speaker was powered by a function generator as discussed in Section 4.2. The frequency of the function generator was electronically varied using an Arduino UNO. A program was developed on LabVIEW to send commands to the Arduino and automatically record the filtered and amplified signal from the microphone.

The procedure used for conducting the measurement generated data to determine both the speed and attenuation for different wave frequencies. The speaker and microphone were initially clamped at a relative separation of 60 cm apart. The peak-to-peak voltage V_{PP} and phase shift $\Delta\phi$ was recorded for different frequencies using the LabVIEW program. The relative separation Δx was incrementally reduced. The new value of Δx was recorded and the measurements repeated until the speaker and microphone meet.

For each frequency, two plots were created. The plot of $\ln(V_{PP})$ against Δx and $\Delta\phi$ against Δx have gradients equal to minus the attenuation coefficient α and the wavenumber k respectively. The speed v of the wave is then $v = \omega/k$ where ω is the angular frequency. By plotting the different values of v and α against frequency, the frequency dependence can be determined.

5 Results and Discussion

In this section, I present the results obtained from the experiment. The calibration of the function generator and the LabVIEW controls are first discussed followed an assessment of the signal-to-noise ratio. Examples of the plots used to determine the wave speed and attenuation coefficient is examined below for a single frequency. It was found that while the wave speed is straightforward to obtain from Figure 10, the plot of $\ln(V_{PP})$ against Δx in Figure 11 displays unexpected behaviour.

5.1 Calibration

The function generator was set up to have a frequency range of 3 kHz to 12 kHz as the control voltage was varied between 0 V to 5 V. Figure 7 shows a linear relationship between the output frequency of the function generator and the control voltage. As the LabVIEW program was used to vary the control voltage, it is also useful to consider the relationship between the voltage command issued by the user to the program versus the actual control voltage. This is shown in Figure 8. We see that the gradient deviates slightly from unity and the intercept is non-zero. This however has no observable effects on quantities derived from the experiment as the frequency of the wave generated by the speaker is directly measured.

5.2 Signal-to-noise Ratio

Efforts were made to reduce noise in the experiment. The signal-to-noise power ratio calculated from the

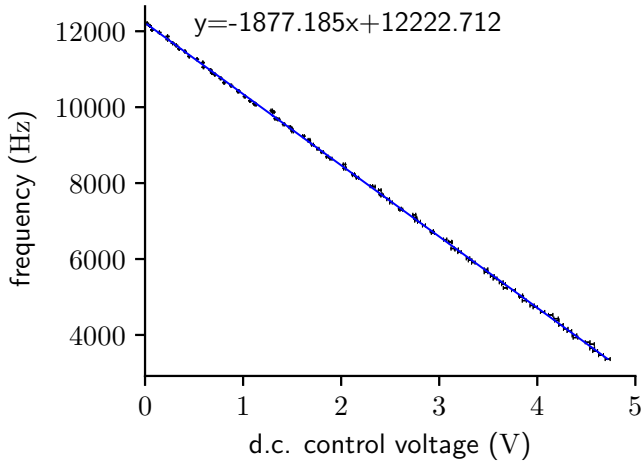


Figure 7: Plot of output frequency against control voltage input to the Black Star Jupiter 2000 function generator.

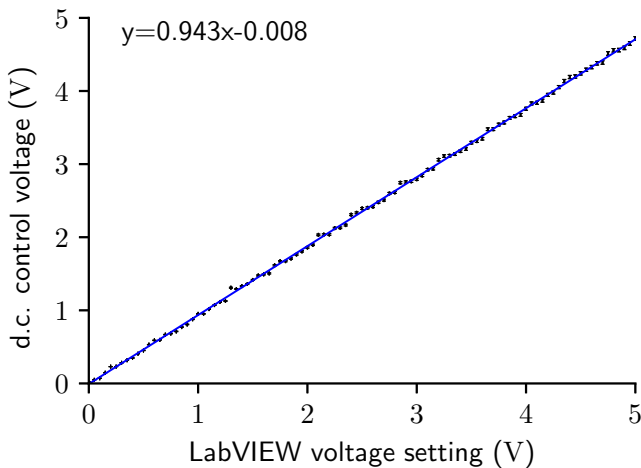


Figure 8: Plot of control voltage against LabVIEW user input.

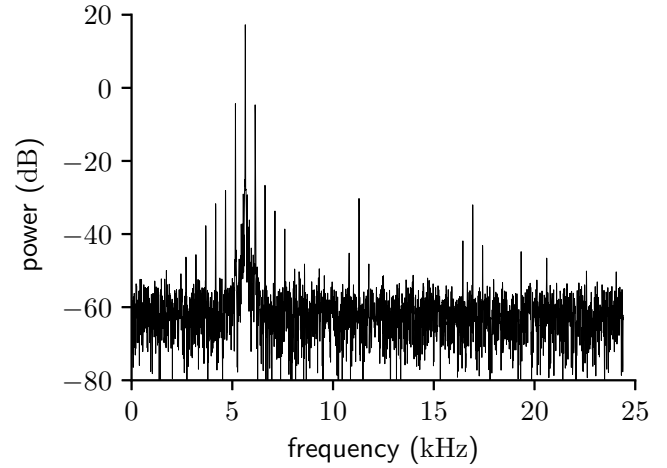


Figure 9: Fourier spectrum of signal recording from electret microphone for (5645 ± 1) Hz signal

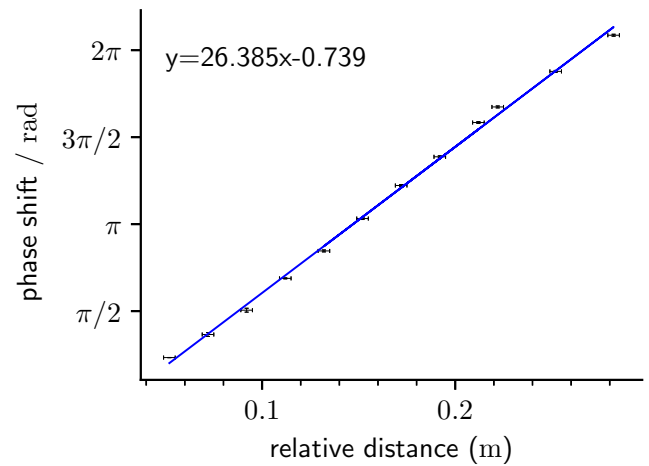


Figure 10: Plot of phase shift against relative separation between input signal to the speaker and detected signal from the electret microphone.

Fourier transform of a (5645 ± 1) Hz signal (Fig. 9) is $\sim 1 \times 10^{-4}$.

5.3 Speed Measurement

The wave speed was calculated from Figure 10. Data was obtained for a (1515 ± 1) Hz wave in air. The speed of sound in air is known to be approximately 343 m s^{-1} . The calculated speed using the method discussed in Section 4.6 was $(344 \pm 1) \text{ m s}^{-1}$ which agrees with the known value.

5.4 Attenuation Measurement

The amplitude A of the wave is expected to exhibit the usual exponential decay of the form $A = A_0 \exp(-\alpha x)$ where A_0 is the initial amplitude of the wave and α is the attenuation coefficient. It is shown in Figure 11 that this naive assumption does not apply in this case.

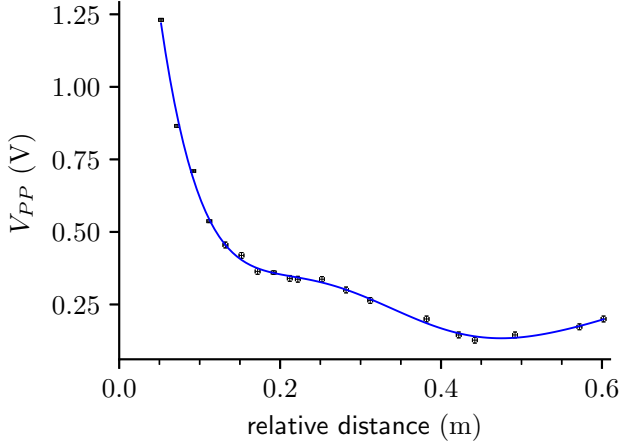


Figure 11: Plot of signal amplitude against relative separation for the on-axis measurement.

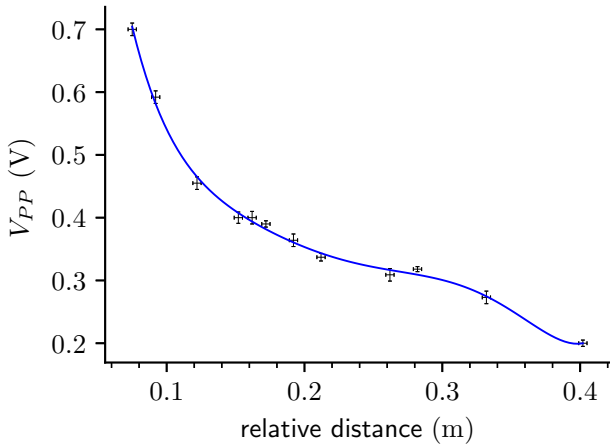


Figure 12: Plot of signal amplitude against relative separation for the off-axis measurement.

The amplitude decreases in a non-exponential fashion up until a relative separation of approximately 40 cm when the amplitude begins to recover.

This unexpected behaviour is suspected to be due to the fact that the wave emitted from the speaker, which is an extended object with finite dimensions, is not a plane wave. Therefore the simple plane wave ansatz $A = A_0 \exp(i\mathbf{k} \cdot \mathbf{x})$ where \mathbf{k} is the complex wavevector and \mathbf{x} is the direction of propagation, does not apply. In hope to grasp the effects of the geometry of the speaker, the experiment was repeated but with the microphone varying along a direction 30° to the normal of the speaker surface. The result is shown in Figure 12. In this off-axis case, the form of the decay is not simply a scaled version of the on-axis one pointing to the possibility that the wavefront is neither planar nor circular but rather has a more complex geometry. The results in Figure 11 and 12 show that the attenuation coefficient cannot be calculated from the current experimental set-

up. It became clear that if one were to attempt to fit an exponential decay to the data and exclude outliers, this would be neglecting the interesting physics that should instead be explored in more detail. At this stage, the experimental aspect of the work had to be paused and we turn our attention instead to a numerical simulation of the wave propagation in soil.

6 Soil as an Unsaturated Porous Medium

We now shift our focus to the secondary aim of the paper, that is, to map out conditions under which a suitable range of detection can be achieved by an acoustic detection device. The detection range depends on how heavily the signal is attenuated as it travels through a medium. The relevant attenuation coefficient is a function of parameters of both the medium and the wave. Here I chose to focus on how the attenuation coefficient depends on the frequency of the wave and the saturation of the soil.

The aim is to build towards a description of unsaturated soil as a three-component poroelastic medium [6]. Saturated porous media consist of two components, soil and water. They are shown to support three types of waves—one shear wave S and two compressional waves, $P1$ and $P2$. The S and $P1$ waves are attributed to the solid skeleton while the $P2$ wave is attributed to the pore fluid. The three-component model for unsaturated porous media extends these by allowing for the existence of a second fluid immiscible with the first. It was shown that a third type of wave, $P3$, emerges due to the capillary pressure between the two fluids [5]. In practice, both $P2$ and $P3$ waves are difficult to measure experimentally as they are heavily attenuated.

In this section, we begin by introducing the important material parameters relating to the composition of the soil. We will see that the dependence of the attenuation coefficient on soil saturation enters through these parameters. Later, the balance laws [12] for the three-component model, presented in the Eulerian picture are introduced.

6.1 Capillary Pressure

Capillary pressure is the pressure that exists at the interface between two immiscible fluids in a thin tube, or in this case the narrow pore spaces between the solid skeleton. The fluid with the higher wettability—the tendency to be adsorbed by the capillary walls—is defined as the wetting phase while the other is defined as the non-wetting phase. In the case of a water-air mixture in sandstone, water is the wetting phase. We define capillary pressure as the pressure difference at the interface of the fluids

$$p_c = p_{non-wetting} - p_{wetting}. \quad (1)$$

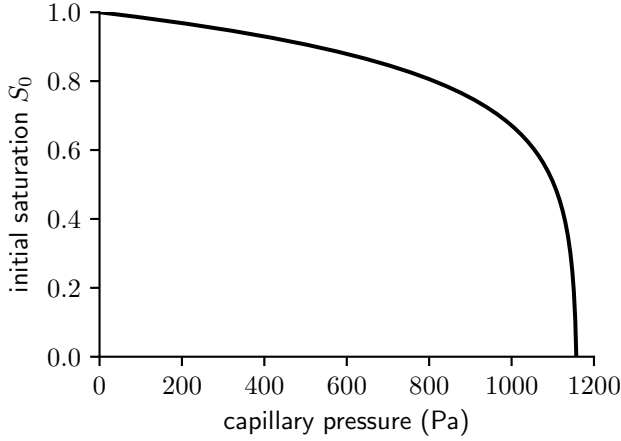


Figure 13: Plot of Santos' capillary pressure.

where p_c is the capillary pressure, $p_{non-wetting}$ and $p_{wetting}$ are the pressures of the two fluid phases.

The dependence of capillary pressure on soil saturation can be obtained empirically through experiments or via closed-form equations such as those proposed by Santos et al. or van Genuchten [7]. The former is chosen for this simulation and is shown in Figure 13.

$$p_c = p_{c_r} e^{-AS_{or}} (e^{-AS_o} - 1)$$

where $A = 6.029158$, $S_{or} = 0.519$, $p_{c_r} = 0.0000026509109 \times 10^9$.

6.1.1 Permeability

The permeability parameter k measures how well a porous medium can transmit fluid. It is related to the hydraulic conductivity K which is a parameter used to describe how easily a certain fluid flows through a particular porous media by

$$k = \frac{K\eta}{\rho g}, \quad (2)$$

where η and ρ are the viscosity and density of the fluid, and g is the acceleration of free fall [27]. While K is dependent on the properties of the fluid, k is a property of the porous material only. K is defined by Darcy's law [14], the porous media analogue to Ohm's law for electrical circuits.

$$\frac{Q}{A} = -K \frac{dh}{dl},$$

where Q is the volumetric flow rate, A is the cross-sectional area through which the fluid flows and dh/dl is the hydraulic gradient. In defining the hydraulic gradient, the concept of hydraulic head must be introduced. The hydraulic head h has units of length and represents the energy per unit weight of the pore fluid due to its elevation and pore pressure [9]. The hydraulic gradient dh/dl is the change in head per unit distance along the direction of greatest change in head. That is to say

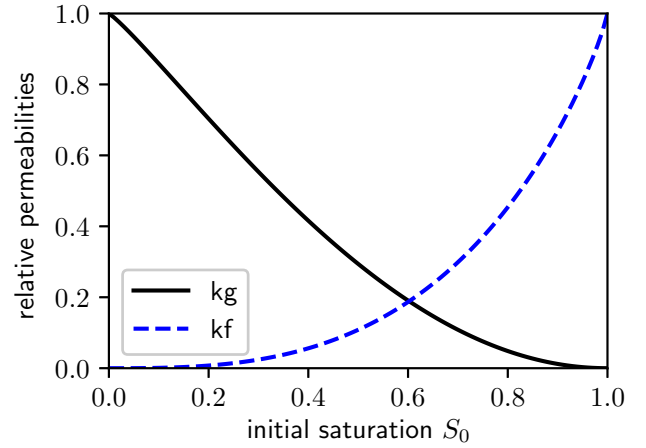


Figure 14: Relative permeabilities against saturation.

that fluid flows in the direction of maximum decrease in hydraulic head.

Wave propagation depends on the resistance parameters π . These are related to the permeability parameter by $\pi = \eta/k$ where η is the viscosity of the fluid and k is the permeability parameter for the soil. This describes the resistance of the porous material against the flow of the fluid. It is assumed that the resistance parameter for the fluid mixture can be separated into the effective resistance for the water and gas

$$\pi^{FS} = \frac{\pi^F}{k^F} \quad \text{and} \quad \pi^{GS} = \frac{\pi^G}{k^G}$$

where π^{FS} and π^{GS} are the effective resistances, π^F and π^G are the experimentally determined resistance parameters of each fluid. k^F and k^G are the relative permeabilities which depend on saturation. The theoretical relationship as proposed by van Genuchten [7] that fits with experimentally determined behaviour [29] are given by

$$k^F = S^{\frac{1}{2}} [1 - (1 - S^{\frac{1}{m}})^m]^2$$

and

$$k^G = (1 - S)^{\frac{1}{2}} (1 - S^{\frac{1}{m}})^{2m}$$

where $m = 0.85$, a fitting parameter. Figure 14 shows the relative permeabilities plot.

6.2 Material Parameters

The final set of parameters are the material parameters $\{\lambda^S + (2/3)\mu^S, F, G, Q^F, Q^G, Q^{FG}\}$. Following the approach used by Detmann [4], these macroscopic material parameters can be derived from a set of microscopic parameters that are dependent on the microstructure of the bulk material. This is done by borrowing the relations from Santos, Corbero and Douglas [23]. In Santos et al.'s approach, the set of material parameters $K_c^*, B_1, B_2, M_1, M_2, M_3$ that were used

Table 2: Summary of material properties chosen for modelling.

	water	gas
$\rho_0^{\theta R}$ (kg m ⁻³)	1000	100
K^θ (Pa)	2.25×10^9	2.2×10^7
μ^θ (mPa s), 20°C	1	0.015

are different from those appearing in the dispersion relations. Detmann shows, however, that these have a simple relationship with the set of parameters $\{\lambda^S + (2/3)\mu^S, F, G, Q^F, Q^G, Q^{FG}\}$ that we wish to evaluate.

Calculating Santos et al.'s parameters with the capillary relation above and mapping the results to the Detmann material parameters yield a relationship between the material parameters and soil saturation. Figure 15 shows the parameters for the case of a sandstone-water-gas mixture. The sandstone skeleton and the pore fluids have the following properties:

$$n_0 = 0.25, \rho_0^{SR} = 2650 \text{ kg m}^{-3}, K^S = 48\,109 \text{ Pa}, \quad (3)$$

$$K^d = \frac{K^S}{1 + gn_0}, g = 50, k = 1 \times 10^{-7} \text{ m}^2 \quad (4)$$

where n_0 is the initial porosity, ρ_0^{SR} is the true density of the material with zero porosity, K^S is the bulk modulus of the grains and K^d is the drained modulus which represents the bulk modulus of the empty matrix. The constant g is a fitting constant that is found by fitting the expression with experimental data obtained from different soil types [28].

Figure 15 shows the behaviour of the material parameters as saturation is varied. The parameter $\lambda^S + (2/3)\mu^S$ is roughly independent of saturation which is expected as this is a property of the solid skeleton and therefore is not influenced by the composition of the pore fluids. The parameters relating to each pore fluid also behave as expected with the sandstone-water coupling constant and the compressibility factor of the water reaching a maximum but finite value when the soil is saturated with water ($S = 1$) and going to zero when there is no water in the pores ($S = 0$). The analogue is true for the parameters relating to the existence of the gas. The coupling constant Q^{FG} between the fluids is zero when either one of the fluids disappears and is maximum near intermediate saturation values.

6.3 Three-Component Model

We now look at the three-component model which incorporates the parameters mentioned above. We begin with the balance laws which arise from continuum mechanics. Continuum mechanics allows us to view the material as a continuous mass rather than as discrete particles [21] through the use of a representative volume element (RVE) defined in Section 3.1. The balance

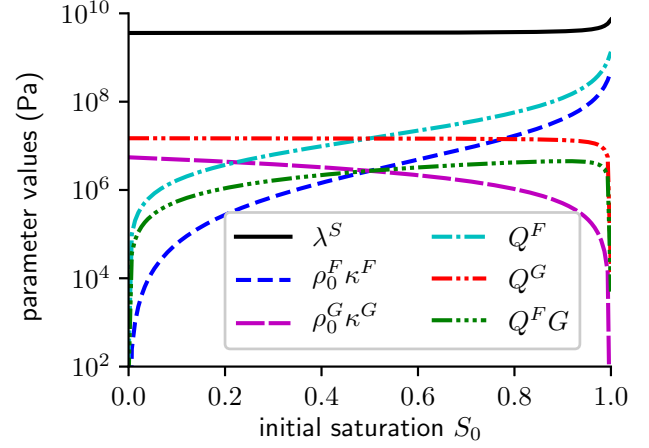


Figure 15: Plot of Detmann's material parameters.

laws capture the idea that the rate of change of a quantity within a volume must be due to one or more of the following—the flow of the quantity through the surface that bounds the volume, a source that is on the boundary and a source that is within the volume itself [12].

To distinguish between the two fluids, let us denote the parameters corresponding to the wetting phase and non-wetting phase with superscripts F and G respectively.

- conservation of mass

$$\frac{\partial \rho^\theta}{\partial t} + \rho_0^\theta \operatorname{div} \mathbf{v}^\theta = 0 \quad \text{where } \theta \in \{S, F, G\} \quad (5)$$

- balance of linear momentum

$$\rho_0^\theta \frac{\partial \mathbf{v}^\theta}{\partial t} = \operatorname{div} \mathbf{T}^\theta + \hat{\mathbf{p}}^\theta \quad \text{where } \theta \in \{S, F, G\} \quad (6)$$

- porosity balance equation

$$\frac{\partial \Delta n}{\partial t} + \phi \operatorname{div} \mathbf{J} = \hat{n}, \quad \Delta n = n - n_{\text{eqm}} \quad (7)$$

Solving the balance equations using appropriate constitutive relations and representing the partial densities instead by volume changes of the components, we end up with the following field equations for the set of essential fields $\{\mathbf{v}^\theta, \mathbf{e}^S, \epsilon^F, \epsilon^G, n\}$ where $\theta \in \{S, F, G\}$ [5]:

$$\begin{aligned}
\rho_0^S \frac{\partial \mathbf{v}^S}{\partial t} &= \text{div} \{ \lambda^S e \mathbf{1} + 2\mu^S \mathbf{e}^S + Q^F \epsilon^F \mathbf{1} + Q^G \epsilon^G \mathbf{1} \} \\
&\quad + \pi^{FS} (\mathbf{v}^F - \mathbf{v}^S) + \pi^{GS} (\mathbf{v}^F - \mathbf{v}^S), \\
\rho_0^F \frac{\partial \mathbf{v}^F}{\partial t} &= \text{grad} \{ \rho_0^F \kappa^F \epsilon^F + Q^F e + Q^{FG} \epsilon^G \\
&\quad - \pi^{FS} (\mathbf{v}^F - \mathbf{v}^S) \}, \\
\rho_0^G \frac{\partial \mathbf{v}^G}{\partial t} &= \text{grad} \{ \rho_0^G \kappa^G \epsilon^G + Q^G e + Q^{FG} \epsilon^F \\
&\quad - \pi^{GS} (\mathbf{v}^G - \mathbf{v}^S) \}, \\
\frac{\partial \mathbf{e}^S}{\partial t} &= \text{sym grad } \mathbf{v}^S, \\
\frac{\partial \epsilon^F}{\partial t} &= \text{div } \mathbf{v}^F, \quad \frac{\partial \epsilon^G}{\partial t} = \text{div } \mathbf{v}^G, \quad e \equiv \text{tr } \mathbf{e}^S \\
n &= n_0 \left[1 + \delta e + \frac{\phi^F}{n_0} (e - \epsilon^F) + \frac{\phi^G}{n_0} (e - \epsilon^G) \right]
\end{aligned}$$

7 Wave Propagation

Wave analysis is done by assuming the following wave ansatz for the essential fields [4]:

$$\begin{aligned}
\mathbf{e}^S &= \mathbf{E}^S \psi, \quad \epsilon^F = E^F \psi, \quad \epsilon^G = E^G \psi, \\
\mathbf{v}^\theta &= \mathbf{V}^\theta \psi \quad \text{where } \theta \in \{S, F, G\}, \\
n - n_0 &= D\psi, \quad \psi \equiv \exp i(\mathbf{k} \cdot \mathbf{x} - \omega t)
\end{aligned}$$

where \mathbf{E}^S , $E^{\{F,G\}}$, $\mathbf{V}^{\{S,F,G\}}$ and D have constant amplitudes, ω is a given frequency and $\mathbf{k} = k\mathbf{n}$ is a wave vector with \mathbf{n} being the unit vector in the direction of propagation.

7.1 Dispersion Relations

The dispersion relations that follow from substituting the wave ansatz into the balance equations [5] are split into the transverse case and the longitudinal case.

Transverse:

$$\begin{aligned}
&\omega^2 \left[1 - \frac{\mu^S}{\rho_0^S} \left(\frac{k}{w} \right)^2 \right] - \pi^{FS} \pi^{GS} \frac{\rho_0^S + \rho_0^F + \rho_0^G}{\rho_0^S \rho_0^F \rho_0^G} \\
&\times \left[1 - \frac{\mu^S}{\rho_0^S + \rho_0^F + \rho_0^G} \left(\frac{k}{w} \right)^2 \right] + i\omega \left\{ \frac{\pi^{FS} + \pi^{GS}}{\rho_0^S} \right. \\
&\left. + \left(\frac{\pi^{FS}}{\rho_0^F} + \frac{\pi^{GS}}{\rho_0^G} \right) \left[1 - \frac{\mu^S}{\rho_0^S} \left(\frac{k}{w} \right)^2 \right] \right\} = 0
\end{aligned}$$

Longitudinal:

$$\sum_{m=0}^2 A_m(\omega) \left(\frac{k}{\omega} \right)^{2m} = 0$$

where the complex coefficients $A_m(\omega)$ are given by:

$$\begin{aligned}
A_0(\omega) &= \omega^2 - \pi^{FS} \pi^{GS} \frac{\rho_0^S + \rho_0^F + \rho_0^G}{\rho_0^S \rho_0^F \rho_0^G} \\
&\quad + i\omega \left(\frac{\pi^{FS} + \pi^{GS}}{\rho_0^S} + \frac{\pi^{FS}}{\rho_0^F} + \frac{\pi^{GS}}{\rho_0^G} \right) \\
A_1(\omega) &= \omega^2 \left(\frac{\lambda^S + 2\mu^S}{\rho_0^S} + \kappa^F + \kappa^G \right) \\
&\quad + \frac{\lambda^S + 2\mu^S}{\rho_0^S} \frac{\pi^{FS} \pi^{GS}}{\rho_0^F \rho_0^G} + \frac{\pi^{FS} \pi^{GS}}{\rho_0^S \rho_0^F \rho_0^G} [\rho_0^F \kappa^F + \rho_0^G \kappa^G \\
&\quad + 2(Q^F + Q^G + Q^{FG})] \\
&\quad - i\omega \left[\frac{\lambda^S + 2\mu^S}{\rho_0^S} \left(\frac{\kappa^F}{\rho_0^F} + \frac{\kappa^G}{\rho_0^G} \right) \right. \\
&\quad \left. + \frac{(\pi^{FS} + \pi^{GS})(\kappa^F + \kappa^G)}{\rho_0^S} \right. \\
&\quad \left. + \frac{\pi^{FS} \kappa^G + \pi^{GS} \kappa^F}{\rho_0^F} + 2 \frac{\pi^{FS} Q^F}{\rho_0^S \rho_0^F} + 2 \frac{\pi^{GS} Q^G}{\rho_0^S \rho_0^G} \right] \\
A_2(\omega) &= \omega^2 \left[\frac{\lambda^S + 2\mu^S}{\rho_0^S} (\kappa^F + \kappa^G) + \kappa^F \kappa^G \right. \\
&\quad \left. - \frac{\rho_0^S Q^F Q^G + \rho_0^F Q^G Q^2 + \rho_0^G Q^F Q^2}{\rho_0^S \rho_0^F \rho_0^G} \right] \\
&\quad + i\omega \left[\frac{\lambda^S + 2\mu^S}{\rho_0^S} \left(\frac{\pi^{FS} \kappa^G}{\rho_0^F} + \frac{\pi^{GS} \kappa^F}{\rho_0^G} \right) \right. \\
&\quad \left. + \frac{(\pi^{FS} + \pi^{GS}) \kappa^F \kappa^G}{\rho_0^S} \right. \\
&\quad \left. - \frac{\pi^{FS}}{\rho_0^S \rho_0^F \rho_0^G} (Q^G + Q^{FG})^2 - \frac{\pi^{GS}}{\rho_0^S \rho_0^F \rho_0^G} (Q^F + Q^{FG})^2 \right. \\
&\quad \left. + 2 \frac{\pi^{GS} \kappa^F Q^G}{\rho_0^S \rho_0^G} + 2 \frac{\pi^{FS} \kappa^G Q^F}{\rho_0^S \rho_0^F} \right] \\
A_3(\omega) &= \omega^2 \left[\frac{\lambda^S + 2\mu^S}{\rho_0^S} \left(\frac{Q^F Q^G}{\rho_0^F \rho_0^G} - \kappa^F \kappa^G \right) \right. \\
&\quad \left. + \frac{Q^F Q^2 \kappa^G}{\rho_0^S \rho_0^F} + \frac{Q^G Q^2 \kappa^F}{\rho_0^S \rho_0^G} \right] \\
&\quad - 2 \frac{Q^F Q^G Q^{FG}}{\rho_0^S \rho_0^F \rho_0^G}
\end{aligned}$$

where λ^S and μ^S are the first and second Lamé constants for the solid grains respectively. The latter is also equivalent to the shear modulus. F and G are the compressibility factor of the two fluids defined as $\kappa = PV_m/RT$ where P is the pressure, V_m is the molar volume, R is the universal gas constant and T is the temperature [19]. By definition, the compressibility factor of an ideal gas is unity. Finally Q^F , Q^G and Q^{FG} are the solid-wetting, solid-non-wetting and wetting-non-wetting coupling constants respectively.

The partial densities are simply related to the real densities of the pure material by:

$$\rho^S = n\rho^{SR}, \quad \rho^F = nS\rho^{FR}, \quad \rho^G = n(1-S)\rho^{GR}$$

8 Simulation of Detection Range

The dispersion relations obtained in the previous section can be solved for the complex wavenumber. The wave velocity and attenuation coefficient can be calculated from the complex wavenumber \mathbf{k} as follows:

$$v = \frac{\omega}{|\text{real}(\mathbf{k})|}$$

$$\alpha = |\text{im}(\mathbf{k})|$$

where v is the phase speed and α is the attenuation coefficient.

In this section, numerical results for a particular sandstone-water-gas mixture are presented. The dispersion relations had been solved for the complex wavenumber k as a function of angular frequency of the wave and soil saturation in the sandstone-water-gas case. The phase speed and attenuation coefficient of the acoustic waves were plotted against soil saturation and against frequency.

8.1 Frequency Dependence

In Figure 18 and 19, the phase speed and attenuation coefficient were plotted against frequency for saturation values $S = [0.2, 0.4, 0.6, 0.8, 0.99999]$ and for each wave mode. The frequency range chosen was the audible range between 20 Hz to 20×10^3 Hz. It can be seen that the values of the attenuation coefficients for the S and $P1$ waves are several orders of magnitude lower than that the $P2$ and $P3$ waves within the frequency range of interest. The $P1$ wave is the fastest of all the wave modes which supports earlier findings that the $P1$ wave is a compressional wave transmitted mainly through the solid skeleton. $P3$ is the slowest wave and is most heavily attenuated as it is due to weak interactions between the pore fluids. The speed of the $P2$ wave when saturation is high roughly corresponds to the speed of sound in water as this wave is primarily transmitted through the water phase.

8.2 Saturation Dependence

In Figure 18 and 20, the phase speed and attenuation coefficient were plotted against saturation for frequency values $S = [20, 100, 1000, 5000, 20000]$ and for each wave mode.

9 Detection Range Map

The detection range for different combinations of saturation and frequency was calculated. The detection range is inversely proportional to the attenuation coefficient. The contour plots of saturation against frequency in Figure 16 and 17 show the detection range for the S and $P1$ waves respectively. As these waves are much less heavily attenuated than the $P2$ and $P3$ waves, they are

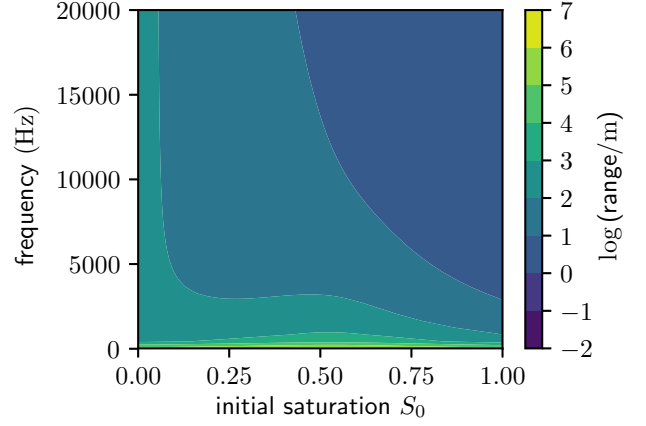


Figure 16: Contour plot of detection range for a matrix of frequency and saturation in the S wave case.

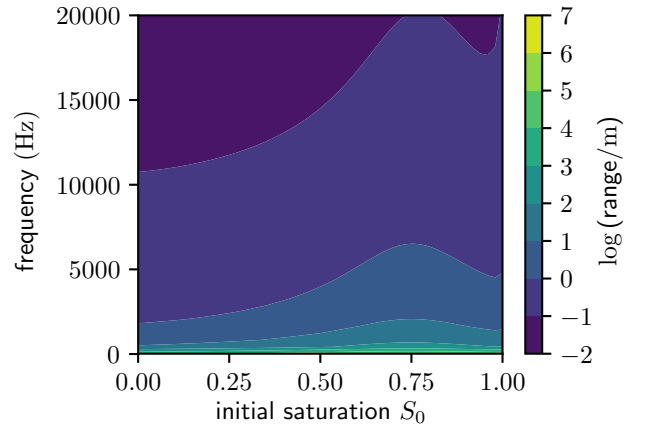


Figure 17: Contour plot of detection range for a matrix of frequency and saturation in the $P1$ wave case.

the most likely waves to be detected in the fields. For frequencies around 3 kHz which are the frequencies of interest for the detection of chafer grubs, we see that the detection range is of order 100 m for the S wave. This behaviour is not observed in practice as the typical detection range was determined in previous work [16] to be approximately 50 cm. The plot for the $P2$ wave, which is the compressional wave transmitted through the soil skeleton, more closely reflects this observation.

10 Conclusion

In this work, we set out to build a device to detect and model the weak signal produced by chafer beetles. It became apparent from the measurement of amplitude decay against relative separation from the source that the model system displays more complex behaviour than originally assumed. A first glance at the form of these amplitude decays, both along the axis normal to the speaker and at an angle, there appears to be geometric

factors that have not been taken into account by the simple plane wave model. Future work may look at whether superposition of effects such as diffraction and reflection off surfaces would be able to predict such an amplitude decay.

Numerical simulation of wave propagation in soil was able to predict detection ranges for different values of soil saturation and wave frequency. For frequencies corresponding to the range present in the spectral analysis of chafer beetle recordings, the range of detection was of order 50 cm for all values of soil saturation.

The findings of this work overall confirms the difficulty in detecting weak signals produced by soil-dwelling insects. Even without loud background noise from wind or vehicles, the fact that soil itself is a composite material with complex microstructures means that more work is needed to understand the different wave modes supported by the medium.

Acknowledgements

I would like to thank Dr Christopher Lester for his thoughtful guidance throughout my entire project and Richard King for his advice on building electrical circuits and his understanding support during the Covid-19 lockdown. I would also like to thank John Flynn and his wife for interesting insights on preparing soil samples and Andy Irvine for lending me several Arduino UNO units for the experiment. Finally, I thank Richard Mankin and Bettina Detmann for providing helpful clarifications in their respective fields of expertise.

Source Code

The source code for this project is available at <https://github.com/tigeryst/ALCBL>.

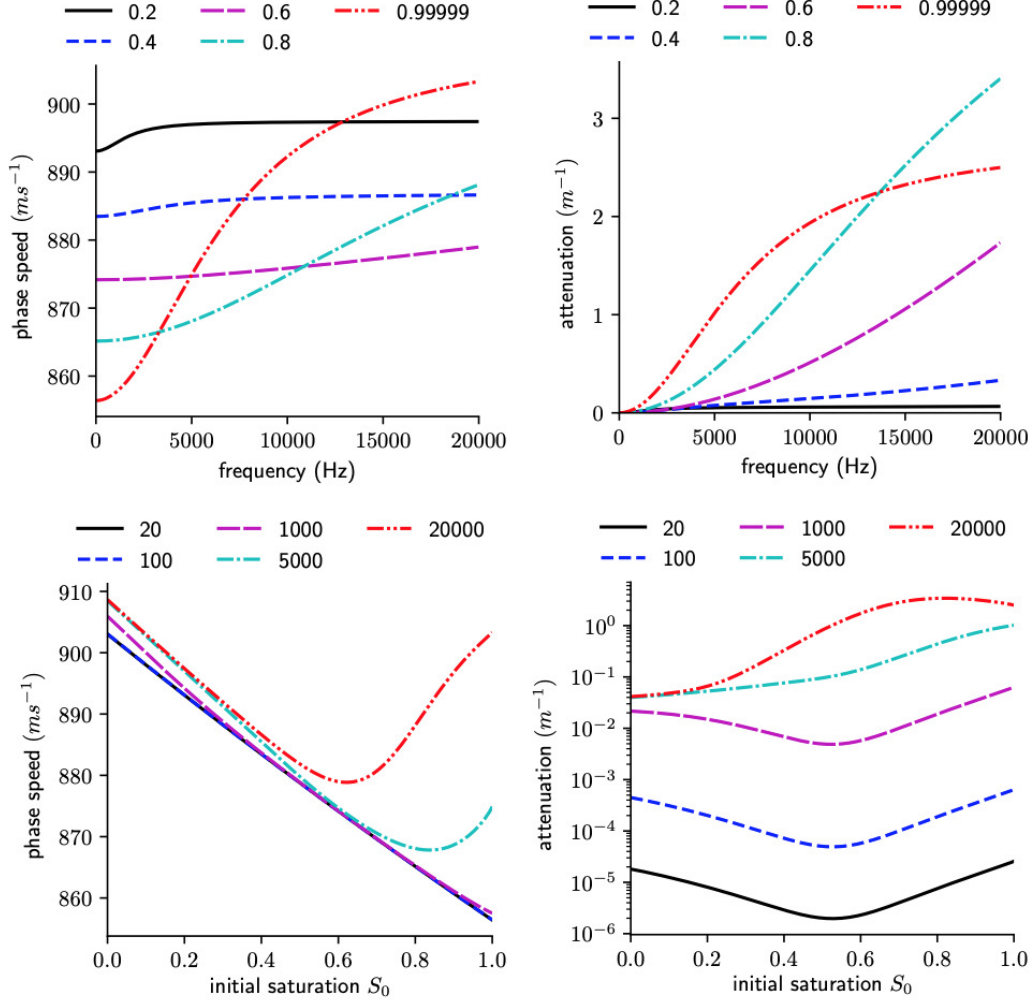
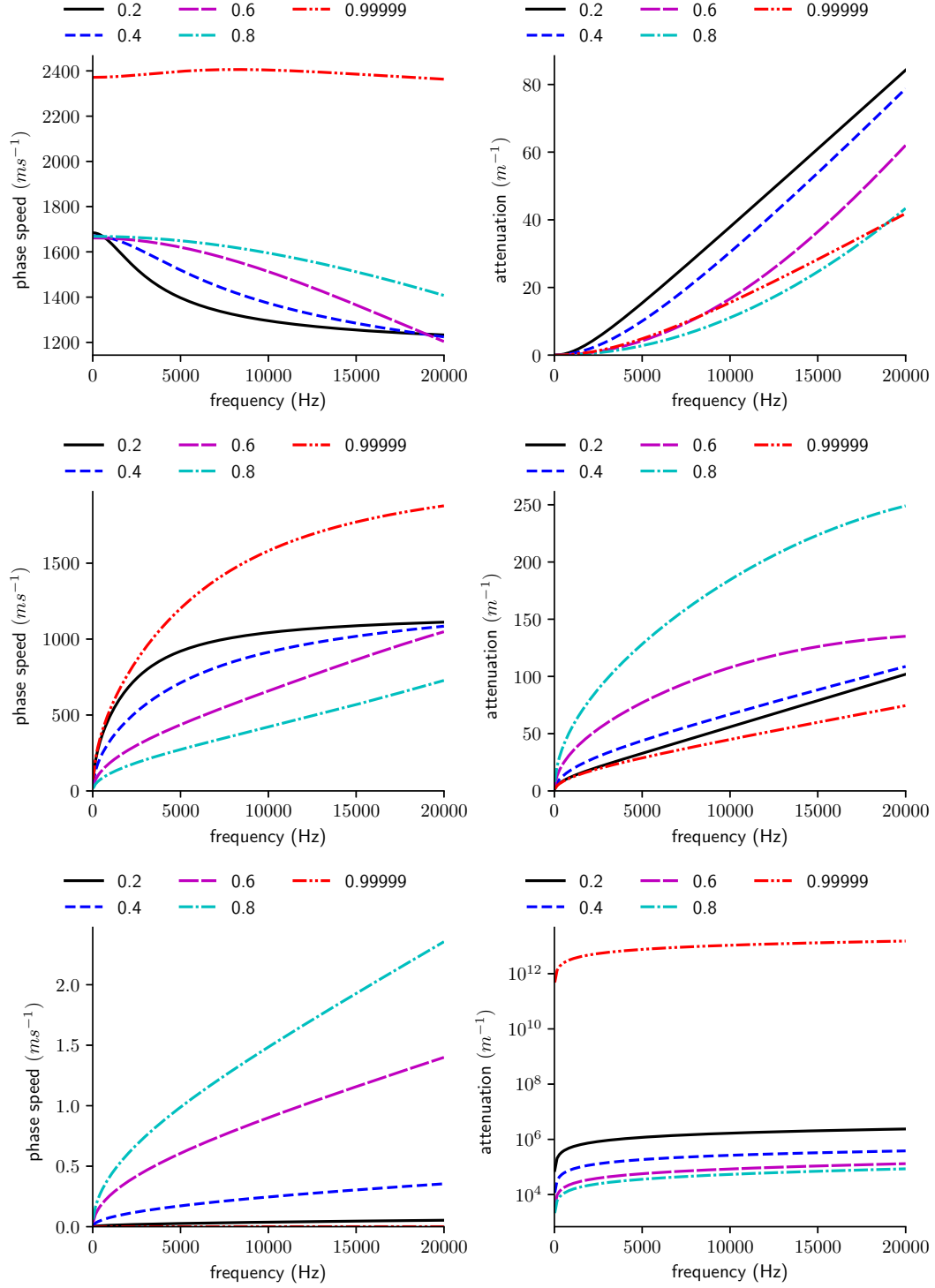
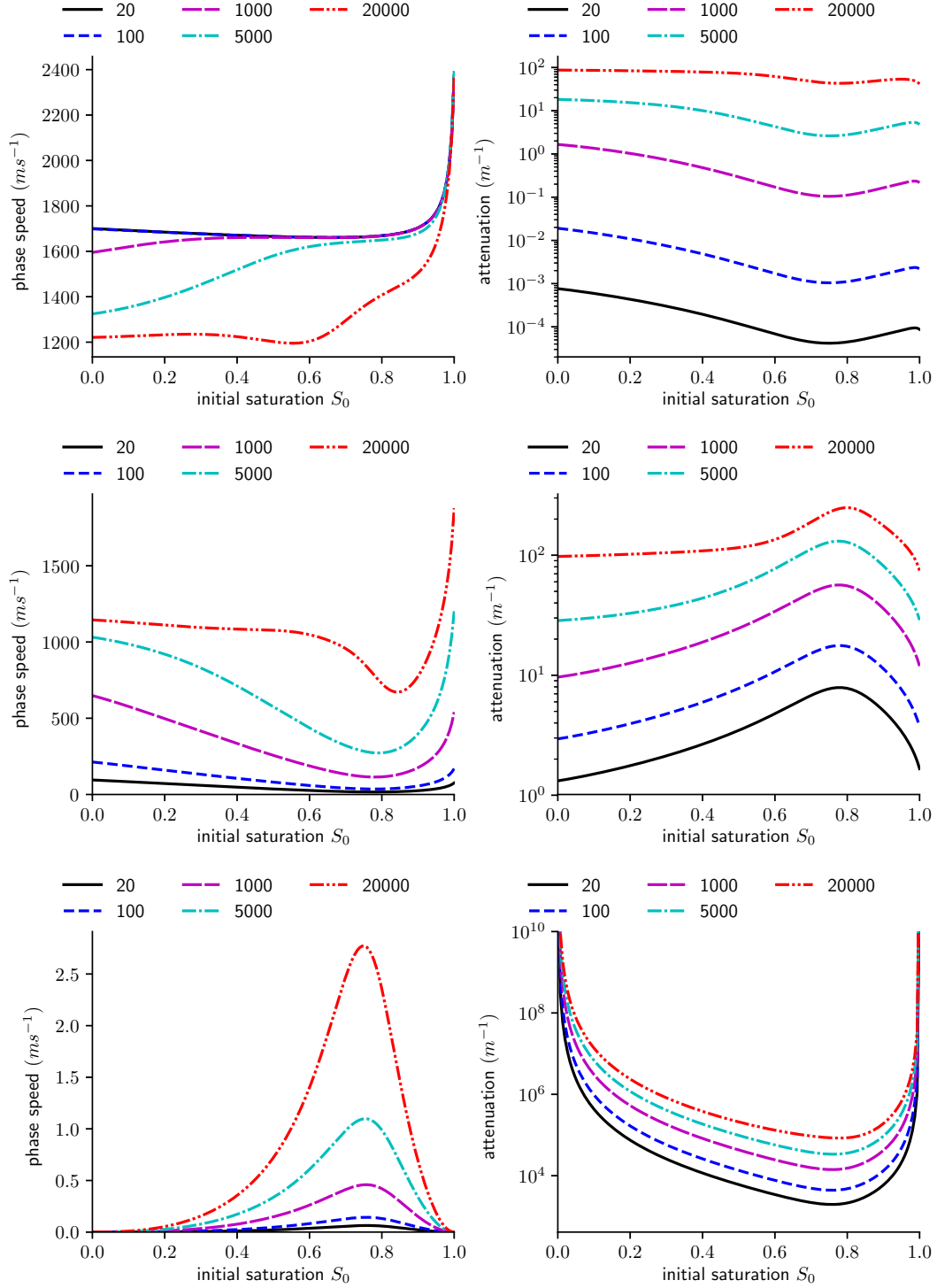


Figure 18: Plot of attenuation and speed against frequency and against saturation for S wave.

Figure 19: Plot of attenuation and speed against frequency. From top to bottom - P_1 , P_2 , P_3 .

Figure 20: Plot of attenuation and speed against saturation. From top to bottom - $P1$, $P2$, $P3$.

References

- [1] 2004. URL: <http://www.landis.org.uk/soilscapes/>.
- [2] D. V. Alford. "Insects". In: *Pests of Ornamental Trees, Shrubs and Flowers: A Color Handbook*. Second. Elsevier Academic Press, 2012, pp. 20–404.
- [3] J. L. Brandhorst-Hubbard et al. "Mapping of Soil Insect Infestations Sampled by Excavation and Acoustic Methods". In: *J. Econ. Entomol.* 94.6 (2001), pp. 1452–1458. DOI: 10.1603/0022-0493-94.6.1452.
- [4] B. Detmann. "Analysis of the Propagation of Sound Waves in Partially Saturated Soils by Means of a Macroscopic Linear Poroelastic Model". In: *Transport in Porous Media* 80.1 (2009), pp. 173–192. DOI: 10.1007/s11242-009-9360-y.
- [5] B. Detmann. "Modeling And Numerical Analysis Of Wave Propagation In Partially Saturated Porous Media". In: *Waves and Stability in Continuous Media* (2008). DOI: 10.1142/9789812772350_0002.
- [6] B. Detmann. "Propagation of Sound Waves in Partially Saturated Soils". In: *Proc. Appl. Math. Mech.* 8.1 (2008), pp. 10667–10668. DOI: 10.1002/pamm.200810667.
- [7] M. T. van Genuchten. "A Closed-form Equation for Predicting the Hydraulic Conductivity of Unsaturated Soils". In: *Soil Sci. Soc. Am. J.* 44.5 (1980), pp. 892–898. DOI: 10.2136/sssaj1980.03615995004400050002x.
- [8] C. Görres and D. Chesmore. "Active Sound Production of Scarab Beetle Larvae Opens Up New Possibilities for Species-specific Pest Monitoring in Soils". In: *Sci. Rep.* 9.1 (2019). DOI: 10.1038/s41598-019-46121-y.
- [9] H. F. Hemond and E. J. Fechner. "The Subsurface Environment". In: *Chemical Fate and Transport in the Environment*. Third. Elsevier Academic Press, 2015, pp. 219–310.
- [10] Rodney Hill. "On Constitutive Macro-variables for Heterogeneous Solids at Finite Strain". In: *Proc. R. Soc. London, Ser. A* 326.1565 (1972), pp. 131–147. DOI: 10.1098/rspa.1972.0001.
- [11] E. I. Inyang et al. "Subterranean Acoustic Activity Patterns of Vitacea Polistiformis (Lepidoptera: Sesiidae) in Relation to Abiotic and Biotic Factors". In: *Insects* 10.9 (2019), p. 267. DOI: 10.3390/insects10090267.
- [12] C. S. Jog. "Balance Laws". In: *Continuum Mechanics: Foundations and Applications of Mechanics*. Cambridge University Press, 2015, pp. 166–202.
- [13] S. N. Johnson et al. "Non-invasive Techniques for Investigating and Modelling Root-feeding Insects in Managed and Natural systems". In: *Agric. For. Entomol.* 9.1 (2007), pp. 39–46. DOI: 10.1111/j.1461-9563.2006.00315.x.
- [14] M. B. Kirkham. "Water Movement in Saturated Soil". In: *Principles of Soil and Plant Water Relations* (2014), pp. 87–101. DOI: 10.1016/b978-0-12-420022-7.00007-0.
- [15] R. W. Mankin, J. L. Brandhorst-Hubbard, and K. L. Flanders. "Acoustic Indicators for Mapping Infestation Probabilities of Soil Invertebrates". In: *J. Econ. Entomol.* 100.3 (2007), pp. 790–800. DOI: 10.1093/jee/100.3.790.
- [16] R. W. Mankin et al. "Eavesdropping on Insects Hidden in Soil and Interior Structures of Plants". In: *J. Econ. Entomol.* 93.4 (2000), pp. 1173–1182. DOI: 10.1603/0022-0493-93.4.1173.
- [17] R. W. Mankin et al. "Methods for Acoustic Detection of Insect Pests in Soil". In: *Soil Sci. Soc. Am. J.* (Nov. 1998), pp. 3–8.
- [18] R. W. Mankin et al. "Perspective and Promise: A Century of Insect Acoustic Detection and Monitoring". In: *American Entomologist* 57.1 (Jan. 2011), pp. 30–44. DOI: 10.1093/ae/57.1.30.
- [19] D. A. McQuarrie and J. D. Simon. *Molecular Thermodynamics*. University Science Books, 1999.
- [20] A. Michelsen et al. "Plants as Transmission Channels for Insect Vibrational Songs". In: *Behavioral Ecology and Sociobiology* 11.4 (1982), pp. 269–281. DOI: 10.1007/bf00299304.
- [21] M. Ostoja-Starzewski et al. "Scaling to RVE in Random Media". In: *Adv. Appl. Math. Mech.* (2016), pp. 111–211. DOI: 10.1016/bs.aams.2016.07.001.
- [22] W. R. Sanders et al. "Acoustic Detection of Arthropod Infestation of Grape Roots: Scouting for Grape Root Borer (Lepidoptera: Sesiidae)". In: *Florida Entomologist* 94.2 (2011), pp. 296–302. DOI: 10.1653/024.094.0224.
- [23] J. E. Santos, J. M. Corberó, and J. Douglas. "Static and Dynamic Behavior of a Porous Solid Saturated by a Two-phase Fluid". In: *J. Acoust. Soc. Am.* 87.4 (1990), pp. 1428–1438. DOI: 10.1121/1.399439.
- [24] D. R. Smitley. "European Chafer". In: *Handbook of Turfgrass Insect Pests*. Entomological Society of America, 2012, pp. 33–35.
- [25] *Soil Types*. 2009. URL: <https://www.rhs.org.uk/advice/profile?pid=179>.
- [26] C. Vincent et al. "Management of Agricultural Insects with Physical Control Methods". In: *Annual Review of Entomology* 48.1 (2003), pp. 261–281. DOI: 10.1146/annurev.ento.48.091801.112639.

- [27] H. F. Wang. *Theory of Linear Poroelasticity: With Applications to Geomechanics and Hydrogeology*. Princeton University Press, 2000.
- [28] J. E. White. *Underground Sound: Application of Seismic Waves*. Elsevier Academic Press, 1983.
- [29] R. D. Wyckoff and H. G. Botset. “The Flow of Gas-Liquid Mixtures Through Unconsolidated Sands”. In: *Physics* 7.9 (1936), pp. 325–345. DOI: 10.1063/1.1745402.